



Article

# Micro-Raman—A Tool for the Heavy Mineral Analysis of Gold Placer-Type Deposits (Pianu Valley, Romania)

Andreea Elena Maftei <sup>1</sup>, Andrei Buzatu <sup>2,\*</sup>, Gheorghe Damian <sup>2</sup>, Nicolae Buzgar <sup>2</sup>, Harald G. Dill <sup>3</sup> and Andrei Ionut Apopei <sup>2</sup>

<sup>1</sup> Institute for Interdisciplinary Research—Science Research Department, Alexandru Ioan Cuza University of Iasi, Lascar Catargi Str. 54, 700107 Iasi, Romania; andreea.maftei@uaic.ro

<sup>2</sup> Department of Geology, Faculty of Geography and Geology, Alexandru Ioan Cuza University of Iași, 20A Carol I Blv., 700505 Iași, Romania; gdamian\_geo@yahoo.com (G.D.); nicolae.buzgar@uaic.ro (N.B.); andrei.apopei@uaic.ro (A.I.A.)

<sup>3</sup> Department of Mineralogy, Gottfried Wilhelm Leibniz University, Welfengarten 1, D-30167 Hannover, Germany; haralddill@web.de

\* Correspondence: andrei.buzatu@uaic.ro

Received: 10 October 2020; Accepted: 5 November 2020; Published: 7 November 2020



**Abstract:** In the current study, different heavy minerals typical of gold placer deposits were identified by means of micro-Raman spectroscopy, and their chemical composition analyzed and discussed (garnet, kyanite, staurolite, zircon, allanite, monazite, xenotime, rutile, anatase, cassiterite, titanite, barite). Even complex solid solution series, such as those of garnets, can be deciphered with the aid of systematic trends observed in Raman line frequencies. The  $\nu_1$  mode in garnets will shift from high to low frequencies as a function of the ionic radius of the  $X^{2+}$  cation, from  $Mg^{2+}$ , to  $Fe^{2+}$  and  $Mn^{2+}$ , while the presence of  $Ca^{2+}$  will make the band to be shifted strongly to even lower wavenumbers. This approach has successfully been taken to differentiate between polymorph triplets such as kyanite-sillimanite-andalusite and rutile-anatase-brookite. Minerals under consideration with high contents of REE, U and Th are affected by intensive metamictization, particularly zircon and titanite. Raman peak features, such as shape, symmetry and intensity, respond to this radiation damage of the lattice and enable fine-tuning of these heavy minerals, such as in the case of fluorite (fetid fluorite).

**Keywords:** Raman spectroscopy; gold placers; heavy minerals; garnet; zircon; allanite; xenotime

## 1. Introduction

Detrital heavy minerals provide insights into the mineral chemistry of the entire source area, and when cast in the role of provenance markers, environment indicators and ore guides, can be successfully used in applied and genetic geosciences [1–5].

Placers are clastic sedimentary deposits formed by mechanical and chemical processes operative in aeolian, fluvial and coastal-marine environments. In particular, weathering of metamorphic, igneous or reworked sedimentary source rocks, sorting on transport and in situ alteration at the trap site play paramount roles during formation of placer-type deposits [6–8]. When it comes to an economic assessment of placer deposits, it is especially gold, platinum group elements (PGE), platinum group minerals (PGM), Ti minerals, zircon and rare-earth elements (REE) minerals that attract the attention of economic geologists and mineralogists [9,10]. There is an ever-increasing demand for heavy minerals worldwide in various branches of the industry, mainly those dealing with new green technologies and

high-tech applications, in addition to the traditional producers of pigments, ceramics, automobiles, glass, nuclear energy, abrasive steel [6,11]. It is not only the quantity of heavy minerals in placer-type deposits, but also their quality that is decisive of whether the raw material can be used for high-end products or only as a high-value commodity. This is where Raman spectroscopy comes in.

High-resolution Micro-Raman spectroscopy is a sensitive technique commonly used in mineral “fingerprinting”, but it also extends to structural, chemical and physical information, which are crucial in genetic and applied geosciences [12,13]. It is a low-destructive method capable of distinguishing the minerals in associations where common polymorphs such as rutile and anatase or calcite and aragonite occur side-by-side with each other [14]. In this case, microprobe analysis has reached its limits, since it cannot differentiate between minerals with the same chemical composition. Moreover, Raman spectroscopy can broaden our knowledge of bond properties that modify even upon slight changes in the chemical composition on a semi-quantitative basis and by considering systematic band shifting [15]. Important structural information can be deduced from the Raman spectra of various classes of minerals: silicates [16–19], phosphates [20,21], sulfates [22,23], sulfides [24–26], or oxides [27–29].

The fundamental vibrational modes of silicate minerals can be described as four types of motions of the main structural units—SiO<sub>4</sub> tetrahedra: (a) nondegenerate  $\nu_1$  symmetric stretching, (b) doubly degenerate  $\nu_2$  symmetric bending, (c) triply degenerate  $\nu_3$  antisymmetric stretching, and (d) triply degenerate  $\nu_4$  antisymmetric bending [30]. Similar modes are also observed in other classes of minerals where the structural units are of tetrahedral type. Besides these fundamental modes, other vibrations appear in the Raman spectra of minerals, such as external or lattice vibrations that are usually noticed in the low region of the spectra.

The aim of the current study is to investigate heavy mineral assemblage typical of placer deposits by means of Raman spectroscopy in order to shed some light on the strong correlation between chemical composition and structural data offered by this technique. Taking this approach requires single-crystal chemical analyses that can confirm certain substitutions and structure deformations that affect the Raman spectra. The results obtained from this information directly translate not only into further investigations regarding source and formation of placer deposits, but also into the economic potential of such mineral accumulations.

## 2. Geological Setting

The Pianu Valley is renowned in Romania for its important alluvial gold deposits. The area has a long-lasting history of gold exploration and exploitation reaching back to antiquity. Traces of panning gold by rudimentary and traditional methods can still be observed today in the environs of Pianu de Sus [31]. Pianu Valley takes an outstanding position as the only site where native platinum has been reported in Romania [32]. The following heavy minerals were identified as major components within the Pianu Valley: garnet, zircon, titanite, magnetite, tourmaline, kyanite, hornblende, Cr-spinel, monazite [32–34].

The Pianu Valley is located in the north-eastern part of the Sebeş Mountains and is made up of Upper Cretaceous and Quaternary sedimentary rocks that rest on the Getic Domain or Median Dacides, according to Săndulescu [35]. In terms of the lithofacies, it belongs to the Sebeş-Lotru variegated litho-group, which is characterized by gneisses, amphibolites, ultrabasic magmatic rocks, quartzites, migmatites, kyanite-bearing micaschists, meso- and epimetamorphic schists, granites, pegmatites and quartziferous porphyries [31,36]. The Getic Realm is intersected by several shear zones [37,38]. These structures are considered as the primary source of the Pianu Valley gold and rare-elements accumulations [32,36,39].

The alluvial–fluvial drainage system spread along the Pianu Valley is Cretaceous in age, and its rocks are denominated as conglomerate, breccia, sandstone, shale, marl, and clay, while the Pleistocene to Holocene deposits include sand, gravel with quartzite boulders [40].

### 3. Materials and Methods

Heavy minerals were sampled in the Pianu Valley area at different locations at which gold occurrences had been identified. The samples were pre-concentrated in the field by manual panning with a 35 cm diameter plastic pan in order to remove as much as possible the light minerals (quartz, feldspars, carbonates). The samples were subsequently enriched in the laboratory using diiodomethane heavy liquid ( $\text{CH}_2\text{I}_2$ ), density of 3.325 g/mL. After the separation procedure with heavy liquid, the resulting fractions consisted of mineral grains with high specific gravity. These heavy mineral fractions were embedded in epoxy resin and prepared as polished sections.

All samples were examined by means of micro-Raman spectroscopy and Electron Probe Microanalysis (EMPA) at Slovak Academy of Sciences from Banská Bystrica, Slovakia. The microprobe measurements were performed on carbon-coated polished sections using the JEOL JXA-8530F. The device operated under an acceleration voltage of 15 kV, 20 nA sample current, 2–5  $\mu\text{m}$  beam diameter, 10–30 s counting time for peaks and 5–15 s for the background. The chemical composition was measured with the following standards and X-ray lines: Nb ( $\text{L}\alpha$ ,  $\text{LiNbO}_3$ ), Si ( $\text{K}\alpha$ , albite), Ti ( $\text{K}\alpha$ , rutile), Al ( $\text{K}\alpha$ , albite), Y ( $\text{L}\alpha$ ,  $\text{YPO}_4$ ), La ( $\text{L}\alpha$ ,  $\text{LaPO}_4$ ), Ce ( $\text{L}\alpha$ ,  $\text{CePO}_4$ ), Pr ( $\text{L}\beta$ ,  $\text{PrPO}_4$ ), Nd ( $\text{L}\alpha$ ,  $\text{NdPO}_4$ ), Sm ( $\text{L}\beta$ ,  $\text{SmPO}_4$ ), Gd ( $\text{L}\beta$ ,  $\text{GdPO}_4$ ), Fe ( $\text{K}\alpha$ , hematite), Mn ( $\text{K}\alpha$ , rhodonite), Mg ( $\text{K}\alpha$ , diopside), Ca ( $\text{K}\alpha$ , diopside), Na ( $\text{K}\alpha$ , albite), K ( $\text{K}\alpha$ , orthoclase), and F ( $\text{K}\alpha$ , fluorite), Si ( $\text{K}\alpha$ , quartz), Mg ( $\text{K}\alpha$ , olivine), Al ( $\text{K}\alpha$ , kyanite), Ti ( $\text{K}\alpha$ , rutile), Cr ( $\text{K}\alpha$ ,  $\text{Cr}_2\text{O}_3$ ).

The Raman spectra were obtained on polished sections using the micro-Raman Spectrometer LabRAM HR800 (Horiba Jobin-Yvon, Kyoto, Japan) coupled with an Olympus BX51 optical petrographic microscope (100 $\times$ /0.80 magnifying objective) and a CCD detector (1024  $\times$  256 pixels). The samples were irradiated using the 632.8 nm excitation line of a He-Ne laser with a power of 17mW. Several density filters were used to prevent from heating, deterioration and fluorescence effect of the samples. The micro-Raman spectra were recorded in the range of 50–1400  $\text{cm}^{-1}$  with an exposure time of 2–20 s per frame, 10–20 acquisitions, in order to improve the signal-noise ratio. Spectral accuracy was calibrated with Rayleigh line and the 520.7  $\text{cm}^{-1}$  line of a Si standard. The system resolution was 2  $\text{cm}^{-1}$ , and the wavenumber accuracy was  $\pm 1 \text{ cm}^{-1}$ . The band fitting and was done by combined Gaussian/Lorentzian amplitude function. The Raman spectra were reduced in intensity for proper display in stacked graphs and better comparison.

### 4. Results and Discussion

Raman investigations of the heavy minerals from the Pianu Valley placer deposit revealed the presence of the following minerals: garnet, kyanite, staurolite, zircon, allanite, monazite, xenotime, rutile, anatase, cassiterite, titanite and barite. All minerals were confirmed by chemical analyses through electron microprobe measurements (EPMA). Their vibrational features are discussed in detail in the next sections.

#### 4.1. Garnets

The garnet group is characterized by the general formula  $\text{X}_3\text{Y}_2(\text{SiO}_4)_3$ , where  $\text{X} = \text{Fe}^{2+}$ ,  $\text{Mg}^{2+}$ ,  $\text{Ca}^{2+}$ ,  $\text{Mn}^{2+}$  and  $\text{Y} = \text{Al}^{3+}$ ,  $\text{Fe}^{3+}$ ,  $\text{Cr}^{3+}$ . Substitutions with other cations may occur in each of these sites, including for  $\text{Si}^{4+}$ , which can be partially substituted by  $\text{Al}^{3+}$ ,  $\text{Ti}^{3+}$ , and  $\text{Fe}^{3+}$  [41]. The structure of these nesosilicates consists of isolated  $\text{SiO}_4$  tetrahedra, together with  $\text{YO}_6$  octahedra and distorted  $\text{XO}_8$  dodecahedra (Figure S1). Besides these three cationic sites, there is also an anionic site for  $\text{O}^{2-}$ ,  $\text{OH}^-$ ,  $\text{F}^-$  [41]. The garnets are divided into two series with six more common members, based on the cation sites occupancy: pyrospites, where  $\text{Y} = \text{Al}^{3+}$ , and  $\text{X} = \text{Mg}^{2+}$  (pyrope-Pyr),  $\text{Fe}^{2+}$  (almandine-Alm),  $\text{Mn}^{2+}$  (spessartine-Spe); and ugrandites, where  $\text{X} = \text{Ca}^{2+}$ , and  $\text{Y} = \text{Cr}^{3+}$  (uvarovite-Uva),  $\text{Al}^{3+}$  (grossular-Gro),  $\text{Fe}^{3+}$  (andradite-And) [41,42].

The chemical analyses show that most of the studied garnets have an almandine-rich composition with variable contents of pyrope, spessartine and grossular (Table S1). The main cation in Y site is  $\text{Al}^{3+}$

(20.65–22.59 wt.%  $\text{Al}_2\text{O}_3$ ), while the X sites are occupied mostly by  $\text{Fe}^{2+}$  with values of FeO ranging from 20.91 to 37 wt.%, with an average of 31.61 wt.%. MgO reaches up to 8.47 wt.%, and MnO has a maximum value of 12.61 wt.%. Variable concentrations of CaO were also observed, with the highest being 9.96 wt.%. Therefore, the analyzed garnets have a calculated composition of  $\text{Alm}_{41-81}$ , which is supplemented either by  $\text{Pyr}_{1-32}$ ,  $\text{Spe}_{0-30}$ , or  $\text{Gro}_{0-28}$ . This gives a variety of intermediate member compositions useful in Raman interpretation of garnet spectra.

Representative Raman spectra are shown in Figure 1, and the Raman bands are listed in Table 1 together with their assignment. The spectra were selected from a total of 27 acquired on different garnet compositions.

The Raman spectra of the studied garnets show three typical regions of frequencies: low region between 162 and 379  $\text{cm}^{-1}$ , a middle interval at 466–639  $\text{cm}^{-1}$ , and high frequency bands between 867 and 1113  $\text{cm}^{-1}$  (Figure 1).

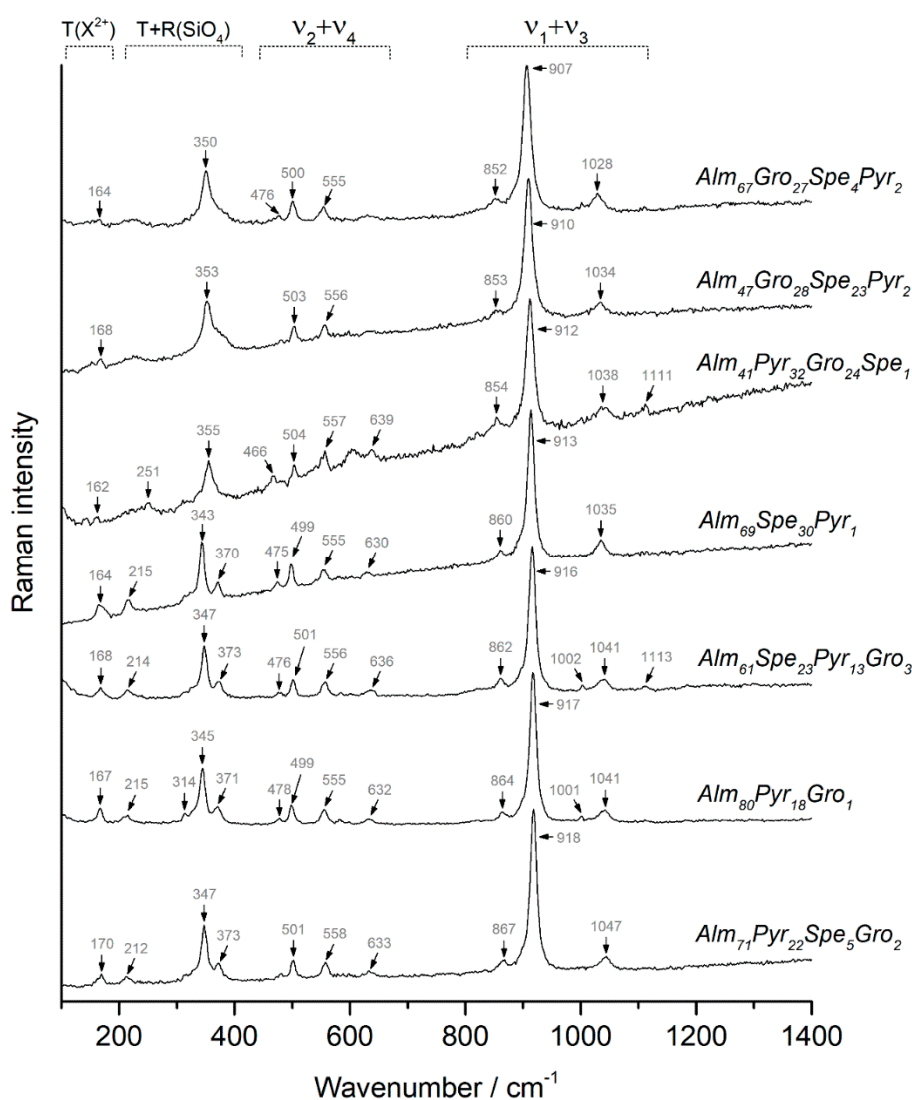


Figure 1. Representative Raman spectra of various garnet compositions and band assignments.

**Table 1.** Raman bands ( $\text{cm}^{-1}$ ) of selected garnet compositions (mol%) and their mode assignments.

Samples/Assignment	01	02	03	04	05	06	07	08	09	10	11
T( $\text{X}^{2+}$ )	164	168	162	168	167	164	168	170	167	167	170
T( $\text{SiO}_4$ )	225		251	214	215	215	214	218	211	215	212
R( $\text{SiO}_4$ )	350	353	355	316 351	314 347	343 370	347 373	318 347	314 345	314 345	347 373
$\nu_2$	476		466	477	478	475	476	479	478	478	482
$\nu_4$	500	503	504	501	500	499	501	501	499	499	501
$\nu_2$	555	556	557	556	555	555	556	558	555	555	558
$\nu_4$			639	634	630	630	636	633	633	632	633
$\nu_3$	852	853	854	858	861	860	862	863	861	864	867
$\nu_1$	907	910	912	915	912	913	916	916	915	917	918
$\nu_3$	1002			1002			1002			1001	
$\nu_3$	1028	1034	1038	1039	1035	1035	1041	1041	1038	1041	1047
$\nu_3$	1110		1111				1113				
Pyr%	2	2	32	18	11	1	13	12	16	18	22
Alm%	67	47	41	66	74	69	61	79	78	80	71
Spe%	4	23	1	2	2	30	23	2	0	0	5
Gro%	27	28	24	14	12	0	3	6	5	1	2

T( $\text{X}^{2+}$ )—translation of X cation; T( $\text{SiO}_4$ )—translation of  $\text{SiO}_4$ ; R( $\text{SiO}_4$ )—rotation of  $\text{SiO}_4$ .

Although the minerals from garnet group have 25 Raman-active modes- $3A_{1g} + 8E_g + 14T_{2g}$  [43], only 14 vibrational modes were observed in the obtained Raman spectra. The bands from the low region of the spectra are attributed to external vibration modes, such as: the peak at  $162\text{--}170\text{ cm}^{-1}$  is assigned to translational modes of  $X^{2+}$  sites, the band at  $211\text{--}251\text{ cm}^{-1}$  to translational motions of  $\text{SiO}_4$  tetrahedra, while the  $313\text{--}318$ ,  $343\text{--}355$  and  $369\text{--}379\text{ cm}^{-1}$  peaks are attributed to rotational modes of  $\text{SiO}_4$ . The medium- and high-frequency regions of the spectra show the internal vibrations of  $\text{SiO}_4$  tetrahedra: O-Si-O bending modes at  $466\text{--}482$ ,  $553\text{--}559\text{ cm}^{-1}$  ( $\nu_2$  symmetric bending) and  $498\text{--}504$ ,  $611\text{--}639\text{ cm}^{-1}$  ( $\nu_4$  antisymmetric bending); Si-O stretching modes at  $907\text{--}918\text{ cm}^{-1}$  ( $\nu_1$  symmetric stretching) and  $852\text{--}867$ ,  $997\text{--}1003$ ,  $1028\text{--}1047$ ,  $1110\text{--}1113\text{ cm}^{-1}$  ( $\nu_3$  antisymmetric stretching). The Raman mode assignments were made according to Bersani et al. [16], Mingsheng et al. [43], Hofmeister and Chopelas [44], Kolesov and Geiger [45], and Kos et al. [46].

A shifting behavior was observed for all Raman peaks based on the chemical composition. These variations are quite complex, since we are dealing with hexary systems such as garnet groups. Furthermore, we will discuss in detail the most intense peak dominating the garnet spectra, which was attributed to  $\nu_1$  vibrational modes of  $\text{SiO}_4$ , as being mostly representative in behavior also of the other bands.

The  $\nu_1$  mode shifts from  $918\text{ cm}^{-1}$  in  $\text{Alm}_{71}\text{Pyr}_{22}$  composition, to  $913\text{ cm}^{-1}$  in  $\text{Alm}_{69}\text{Spe}_{30}$ , to  $907\text{ cm}^{-1}$  in  $\text{Alm}_{67}\text{Gro}_{27}$  (Figure 1). Since the Alm% content remains constant, the Raman line basically decreases in frequency from pyrope to spessartine to grossular. Moreover, intermediate compositions of three end-members place their Raman line between these frequencies:  $916\text{ cm}^{-1}$  for  $\text{Alm}_{61}\text{Spe}_{23}\text{Pyr}_{13}$ ,  $912\text{ cm}^{-1}$  for  $\text{Alm}_{41}\text{Pyr}_{32}\text{Gro}_{24}$  and  $910\text{ cm}^{-1}$  in the case of  $\text{Alm}_{47}\text{Gro}_{28}\text{Spe}_{23}$  (Figure 1). The frequencies of  $\nu_1(\text{SiO}_4)$  mode seem to be significant correlated in a positive way with MgO ( $r = 0.48$ ) and FeO ( $r = 0.51$ ) concentrations, and negatively with CaO ( $r = -0.78$ ), suggesting a shifting to higher wavenumbers as MgO and FeO contents increase, while CaO strongly decreases the line frequency. The same correlations were observed for the calculated Alm% ( $r = 0.46$ ), Pyr% ( $r = 0.51$ ) and Gro% ( $r = -0.79$ ) compositions.

For a better understanding of these peak variations, it has to be considered that line shifting in pyrope-almandine-spessartine-grossular series is caused by atomic mass, atomic structure, ionic radius and polarization of  $X^{2+}$  cations, which strongly affect the unit-cell size and bonds force constants in the crystal structure [43,46]. Out of all these factors, the ionic radius has the strongest influence on the position of the Raman peaks. In pyrope-almandine-spessartine-grossular series, the ionic radii increase from  $\text{Mg}^{2+}_{(0.89)}$  to  $\text{Fe}^{2+}_{(0.92)}$ ,  $\text{Mn}^{2+}_{(0.96)}$  and  $\text{Ca}^{2+}_{(1.12)}$  Å. Therefore, the  $\nu_1$  mode will shift from high to low frequencies from  $\text{Mg}^{2+}$ , to  $\text{Fe}^{2+}$  and  $\text{Mn}^{2+}$ , while the presence of  $\text{Ca}^{2+}$  will cause the band to be shifted strongly to even lower wavenumbers because of the much larger ionic radius [17]. This decrease of the wavenumbers with increasing ionic radius is also supported by the correlations with the chemical results discussed above.

Since in the case of garnets solid solutions we are dealing with four different cations that can substitute each other and form mixed intermediate members, it is important to consider how much each cation contributes with its ionic radius to the  $X^{2+}$  site occupancy. By calculating a weighted average of the ionic radii and molar ratios for each garnet composition, it can be observed that it strongly correlates with the measured Raman  $\nu_1$  mode wavenumbers ( $r = -0.86$ ). This value can be calculated as  $(r_{\text{Mg}} \cdot x_{\text{Pyr}} + r_{\text{Fe}} \cdot x_{\text{Alm}} + r_{\text{Mn}} \cdot x_{\text{Spe}} + r_{\text{Ca}} \cdot x_{\text{Gro}})$ , where  $r$  is the ionic radius and  $x$  represents the mol% of each end-member. Another similar approach is to use the  $\nu_1$  mode frequencies of pure end-members as standard values weighted by their molar ratio. The  $\nu_1$  band appears at  $926\text{ cm}^{-1}$  in pyrope,  $915\text{ cm}^{-1}$  in almandine,  $907\text{ cm}^{-1}$  in spessartine, and  $879\text{ cm}^{-1}$  for grossular [16]. Within this study, by using these values together with the end-members' mol%, a very good correlation with the real frequencies of the  $\nu_1$  mode was observed ( $r = 0.88$ ). This confirms that by applying this procedure backwards and taking into account up to six peaks with unimodal behavior, one can roughly estimate the chemical concentration of any garnet intermediate member using only the Raman analyses, as previously discussed in more detail by Bersani et al. [16] and Smith [17].

As for the other vibrational modes that are present in the Raman spectra of the studied garnets, it was noticed that  $\nu_3(\text{SiO}_4)$  modes at 852–867, 1028–1047  $\text{cm}^{-1}$ ,  $\nu_2(\text{SiO}_4)$  modes at 466–482, 553–559  $\text{cm}^{-1}$ , and  $T(X^{2+})$  mode at 162–170  $\text{cm}^{-1}$  show a similar trend as the already discussed  $\nu_1(\text{SiO}_4)$  vibrations. An inverse behavior was noticed for the peaks at 211–251, 343–355 and 369–379  $\text{cm}^{-1}$ , which are assigned to  $R,T(\text{SiO}_4)$ . The other peaks show no direct correlation with the chemical data, most likely having a multi-modal character.

#### 4.2. Kyanite and Staurolite

Kyanite ( $\text{Al}_2\text{SiO}_5$ ) and staurolite ( $\text{Fe}_2\text{Al}_9\text{Si}_4\text{O}_{23}(\text{OH})$ ) are both nesosilicate minerals (Figures S2–S3). Kyanite is the high-pressure phase of the three  $\text{Al}_2\text{SiO}_5$  polymorphs (sillimanite, andalusite, kyanite), and its structure involves  $\text{Al}^{3+}$  octahedra linked by  $\text{Si}^{4+}$  and  $\text{Al}^{3+}$ . In the case of staurolite,  $\text{Al}^{3+}$  also occupies octahedral sites, and  $\text{Fe}^{2+}$  and  $\text{Si}^{4+}$  have tetrahedral coordinations [47].

The Raman spectra of kyanite (Figure 2) show a large number of clear and sharp peaks, especially in the low wavenumber region. The bands from the 892–1001  $\text{cm}^{-1}$  interval can be attributed to the  $\nu_1$  and  $\nu_3$  stretching modes of  $\text{SiO}_4$  (symmetric and antisymmetric). Two extra peaks were observed in the studied samples at 1113 and 1185  $\text{cm}^{-1}$  (Figure 2—kyanite 2). As for the  $\nu_2$  and  $\nu_4$  bending modes, these appear in the spectra between 607 and 669  $\text{cm}^{-1}$  [19,47]. The strong peak at 485–487  $\text{cm}^{-1}$  can be assigned to bending vibrations of Al-O-Si bonds, as suggested by Zhai et al. [19]. In the low region of the spectra, below 450  $\text{cm}^{-1}$  there are several Raman bands that probably also overlap with the external modes. Zhai et al. [19] assigned these bands to Al-O bending modes and explained it as a cause of poor symmetry and degeneracy in the kyanite structure.

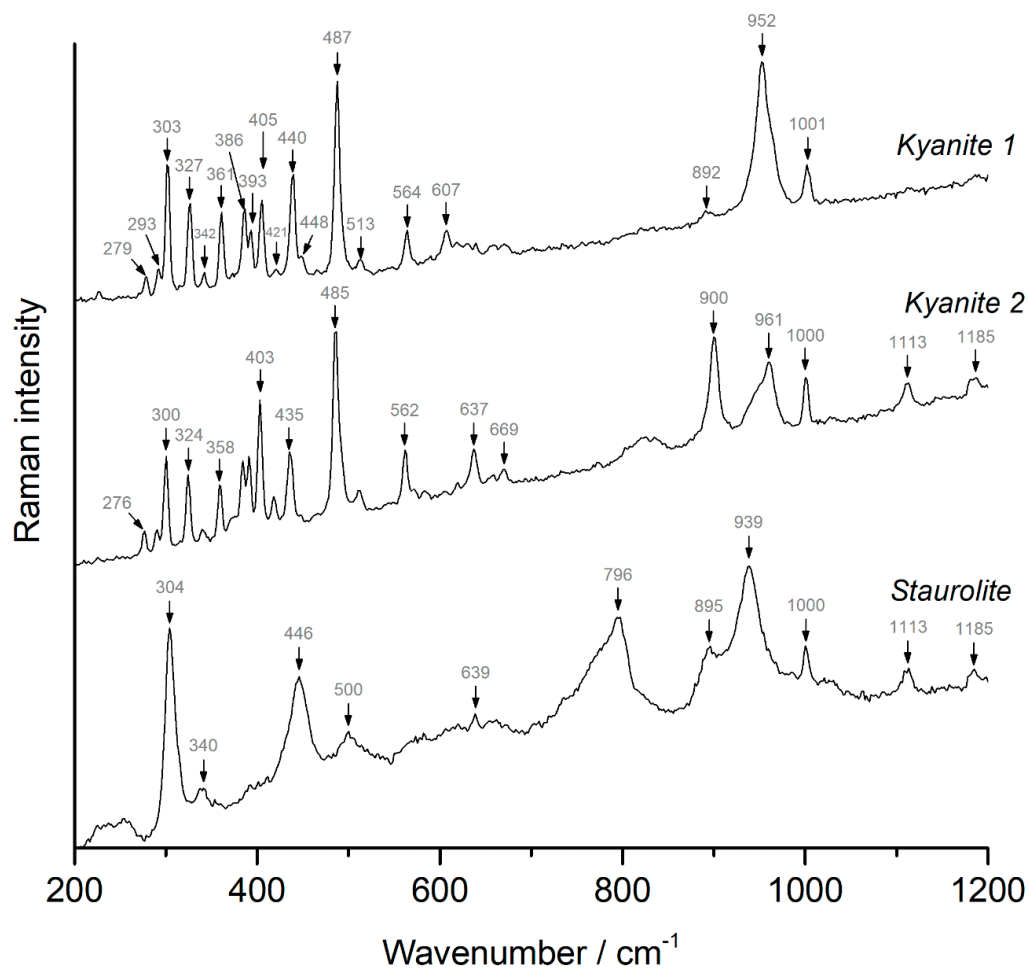


Figure 2. Raman spectra of kyanite and staurolite.

Some differences were observed between kyanite Raman spectra from different analyzed samples. For instance, all peaks from the 200–564  $\text{cm}^{-1}$  region seem to be shifted  $\sim 3 \text{ cm}^{-1}$  (Figure 2—kyanite 1 and 2). Instead, the stretching modes showed an opposite trend: from 892 to 900  $\text{cm}^{-1}$  and 952 to 962  $\text{cm}^{-1}$ . Although the last-mentioned peak might be in fact two overlapping bands with varying intensities (sample orientation), the clear shifting of the other lines might be explained by a slight change in chemical composition. As the EPMA results showed (Table S2), the kyanite 2 sample has a higher content of FeO (0.29 wt.%) and  $\text{TiO}_2$  (0.11 wt.%), which might cause structure deformations. Nevertheless, the Raman spectroscopy proved again to be very useful in identifying kyanite out of the other polymorphs (sillimanite and andalusite) based on structural features, since the chemical analyses were not enough to clearly differentiate between them.

The Raman spectra of the staurolite samples show less peaks than kyanite and have a lower quality with rather broad bands and background noise (Figure 2). This is due to the overlapping modes and the low degree of crystallinity of the analyzed staurolite samples. A similar spectrum was reported previously by Makreski et al. [47], but with some differences in peak positions. According to the assignment of those authors, the peaks observed at 895, 939 and 1000  $\text{cm}^{-1}$  can be attributed to the stretching modes of  $\text{SiO}_4$  tetrahedra, while the bending vibrations occur at 639 and 796  $\text{cm}^{-1}$ . The peaks from the low region of the spectra appear between 304 and 500  $\text{cm}^{-1}$  and might be assigned to Al-O vibrational modes.

The analyzed staurolites suggest a shifting of the 939  $\text{cm}^{-1}$  band to lower wavenumbers in samples with increasing  $\text{TiO}_2$  concentrations correlated with a decreased ZnO, FeO and MgO content, while the other peaks maintain the same frequencies.

### 4.3. REE Minerals

Among the minerals enriched in rare earth elements (REE), zircon, allanite, monazite and xenotime were identified in the heavy mineral fractions of Valea Pianu samples.

Zircon ( $\text{ZrSiO}_4$ ) has a nesosilicate structure with chains of alternating  $\text{SiO}_4$  tetrahedra and  $\text{ZrO}_8$  triangular dodecahedra along the *c* axis (Figure S4) [48,49]. Although zircon is not a true REE mineral, it can accommodate high quantities of REE, Li, P, Y, Ti, Hf, U, and Th in its structure [50]. Allanite-(Ce) belongs to epidote group and has the chemical formula  $\text{CaCe}(\text{Al}_2\text{Fe}^{2+})(\text{Si}_2\text{O}_7)(\text{SiO}_4)\text{O}(\text{OH})$ . Similar species are allanite-(La), allanite-(Y) and allanite-(Nd), depending on the main rare earth element from its structure (Figure S5) [51]. Most allanites can also incorporate the radioactive elements Th and U. Monazite ((Ce, La, Nd, Sm) $\text{PO}_4$ ) and xenotime ( $\text{YPO}_4$ ) are both phosphate minerals that, in places, preferentially accommodate light rare earth elements (LREE), in the case of monazite, and heavy rare earths (HREE), in the case of xenotime, as well as significant amounts of Th and U, in their lattice [20,52]. The monazite structure consists of alternating (REE) $\text{O}_9$  polyhedra and  $\text{PO}_4$  tetrahedra chains parallel to *c* axis [20], while xenotime is isostructural with zircon (Figures S6–S7) [52].

#### 4.3.1. Zircon

The Raman spectra acquired on the studied zircons show some differences, as indicated in Figure 3. The most intense peaks appear at 352–358, 437–440 and 1002–1009  $\text{cm}^{-1}$ . The 1002–1009  $\text{cm}^{-1}$  band is attributed to the  $\nu_3$  stretching mode of  $\text{SiO}_4$  tetrahedra, while the  $\nu_1$  mode was observed at 970–974  $\text{cm}^{-1}$ . Another internal mode was identified at 437–440  $\text{cm}^{-1}$  that was assigned to the  $\nu_2$  bending vibration [18,48,49,53,54]. The 352–358  $\text{cm}^{-1}$  line was previously assigned to the  $\nu_4$  bending mode [55], but more detailed studies based on group-theory analysis of the total number of Raman-active modes and structural investigations concluded that this line is due to external rotational modes of  $\text{SiO}_4$  [18,48,49,53]. The bands from the low region of the spectra, 202, 214 and 224  $\text{cm}^{-1}$  are also attributed to the external modes [49]. Additional bands were observed (Figure 3) which are not consistent with those reported in the literature and might be caused by sample impurities.



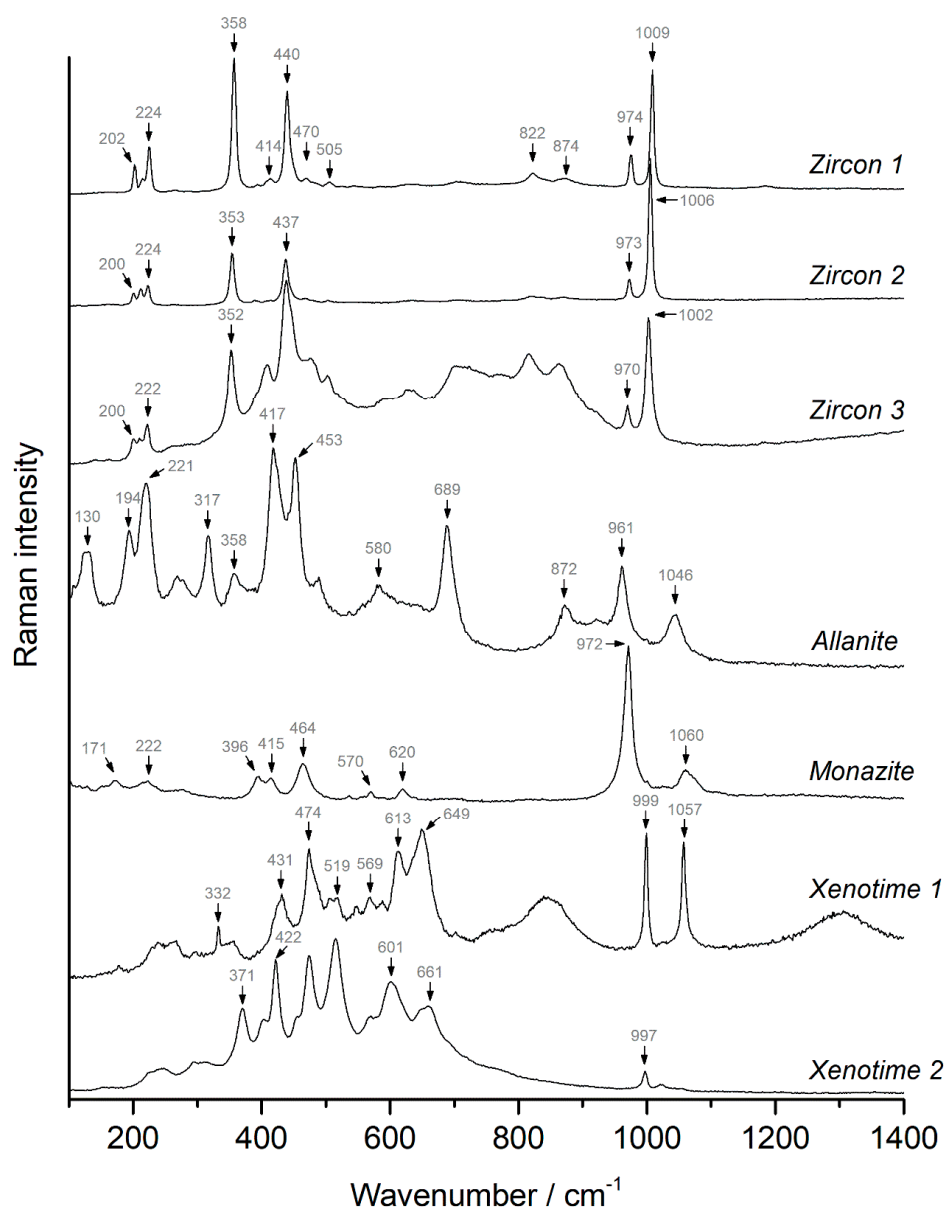


**Figure 3.** The Raman spectra of selected REE minerals: zircon, allanite, monazite and xenotime.

There are some differences to be observed in the Raman spectra of the zircons under study that are considered a result of metamictization. Since natural zircon contains significant amounts of U and Th, the structure can strongly be damaged in the course the bombardment of alpha particles during the radioactive decay [18,48,49]. The metamict zircons have a high degree of structural disorder and consist of a mixture of defect-rich clusters with amorphous regions on a submicrometric scale [18]. These structural changes occur as point defects, SiO<sub>4</sub> tetrahedra polymerization, appearance of ZrO<sub>2</sub>, and even a complete transformation to an amorphous state. The metamict zircons were extensively studied by means of Raman spectroscopy [18,48,49], and it was observed that the degree of damage is reflected by a broadening of the Raman bands, lower peak intensities and lines shifting to smaller wavenumbers. Fresh zircons display sharp and well resolved peaks as those represented in Figure 3—zircon 1 and 2. Therefore, zircon 3 crystal (Figure 3) might be affected by a certain degree of metamictization due to its broader Raman bands observed at lower frequencies. Looking at its chemical composition (Table S3) the U and Th contents are relatively low (0.07 wt.% UO<sub>2</sub> and 0.01 wt.% ThO<sub>2</sub>). Out of all analyzed zircons, the one with the highest U and Th values (0.16 wt.% UO<sub>2</sub> and 0.10 wt.% ThO<sub>2</sub>) shows shifted peaks at lower frequencies as well (i.e.,  $\nu_3$  mode—1005 cm<sup>-1</sup>). Judging from its

very clear spectrum and sharp Raman lines, it can be considered that its structure is less damaged. This might suggest that the line shifting may appear even in non-metamict zircons, but it's actually due to substitutions in cationic site which are causing structural deformations. This radiation damage of the crystal structure can also be observed in the Raman spectra of common ore mineral called fetid fluorite, a heavy mineral scattered in the clastic apron around U-bearing fluorite deposits [56]. The name has been derived from native fluorine in the lattice which spreads a garlic-like smell.

#### 4.3.2. Allanite

Allanite was identified in the present study as a single crystal with three different compositional zones. The mineral is of allanite-(Ce) type, with Ce being partially substituted by La and Nd. The literature data is very limited concerning the Raman studies of allanite. Lopez and Frost [51] reported the Raman spectrum of an "allanite" sample, but their results are considerably different from those obtained in the present study. Most likely, the authors misidentified their sample, since no chemical or X-ray analyses can confirm their assumption. The Raman spectra of allanite identified in Valea Pianu samples (Figure 3) better resemble a Cr-rich allanite-group mineral reported by Varlamov et al. [57], and the Raman frequencies fit perfectly with those reported by Chukanov and Viganina [58] for allanite-(Ce). A tentative assignment of the Raman modes can be made by comparing it with epidote spectrum [59]. Therefore, the observed peaks in the high-frequency region (872, 961 and  $1046\text{ cm}^{-1}$ ) can be attributed to the symmetric and antisymmetric stretching modes of Si-O<sub>nb</sub> (O<sub>nb</sub>—non-bridging oxygens). The stretching vibrations of Si-O<sub>b</sub>-Si (O<sub>b</sub>—bridging oxygens) appear in the spectrum at  $689\text{ cm}^{-1}$ . The two strong bands at 417 and  $453\text{ cm}^{-1}$  and one at  $489\text{ cm}^{-1}$  could be assigned to the bending modes of Si-O<sub>b</sub>-Si bonds. It can be considered that the Raman lines below  $400\text{ cm}^{-1}$  are due to the external modes of M-O interactions. These modes are observed at 130, 194, 221, 269, 317 and  $358\text{ cm}^{-1}$  (Figure 3). No peak shifting was observed in the spectra that might be due to different chemical composition.

#### 4.3.3. Monazite

The Raman spectrum of monazite shows typical features of phosphate minerals (Figure 3). The spectra are dominated by the intense line at  $972\text{--}975\text{ cm}^{-1}$  that is assigned to symmetric stretching  $\nu_1$  modes of PO<sub>4</sub> units while the antisymmetric  $\nu_3$  stretch is observed at  $1055\text{--}1060\text{ cm}^{-1}$ . The bending vibrations are attributed to the Raman bands from 620 and  $570\text{ cm}^{-1}$  ( $\nu_4$  modes) and from  $464\text{--}472\text{ cm}^{-1}$  ( $\nu_2$  modes). The remaining lines that appear below  $450\text{ cm}^{-1}$  are due to the external or lattice modes that involve M-O movements: 171, 222, 396 and  $415\text{ cm}^{-1}$  [20,21,60,61].

Some differences were observed in the Raman lines position for the measured monazites, especially for the symmetric modes  $\nu_1$  ( $972\text{--}975\text{ cm}^{-1}$ ) and  $\nu_2$  ( $464\text{--}472\text{ cm}^{-1}$ ). The studied samples are monazite-(Ce) with additional La, Nd and Th. It seems that there is a systematic shifting caused by the dominant cation that occupies M site. The stretching bands tend to shift to higher wavenumbers with the decrease of ionic radius of the main cation or with its increasing atomic number in the case of REE [20]. For the monazite with the highest frequency of the  $\nu_1$  mode ( $975\text{ cm}^{-1}$ ), it was measured to have the highest content of Y (2.04 wt.% Y<sub>2</sub>O<sub>3</sub>), which has a smaller ionic radius (Table S4).

#### 4.3.4. Xenotime

The Raman measurements of the xenotime samples revealed two slightly different types of spectra (Figure 3). The symmetric stretching  $\nu_1$  is observed at  $997\text{--}999\text{ cm}^{-1}$  and the  $\nu_3$  mode at  $1057\text{ cm}^{-1}$ . The Raman bands at 569, 601–613 and  $649\text{--}661\text{ cm}^{-1}$  can be attributed to  $\nu_4$  antisymmetric bending modes, while the symmetric ones appear at 422–431, 474 and  $519\text{ cm}^{-1}$ . The external modes are observed below  $400\text{ cm}^{-1}$  [60,62].

The Raman spectrum of xenotime 2 type (Figure 3) shows the  $\nu_1$  mode at a decreased intensity and lower frequency ( $997\text{ cm}^{-1}$ ), while the  $\nu_3$  mode is completely diminished. Similar behavior was reported by Švecová et al. [52] for an altered xenotime affected by radiation damage with a high

sub-micrometer porosity. An alteration state of xenotime 2 might explain the different shape of the spectrum. Moreover, the xenotime 2 sample has lower concentrations of U, Th and Y, most likely being leached due to its advanced degree of alteration.

#### 4.4. Oxides

The oxides identified in the Valea Pianu gold deposit by means of Raman spectroscopy are rutile, anatase and cassiterite (Table S5). Titanium dioxides occur in nature as three polymorphs: the stable phase rutile, and metastable anatase and brookite ( $\text{TiO}_2$ ). Rutile and anatase are both tetragonal with different space groups (Figures S8–S9). Tin dioxide has a rutile-like crystalline structure (Figure S10) and it is known as cassiterite ( $\text{SnO}_2$ ).

The Raman spectra of the studied oxides show well-resolved and intense peaks (Figure 4). These bands can be assigned in terms of factor group analysis. Therefore, rutile has four Raman-active modes with symmetries  $B_{1g}$ ,  $E_g$ ,  $A_{1g}$  and  $B_{2g}$ , out of which the  $B_{2g}$  mode has a very low intensity, and it can appear as a weak band at  $827\text{ cm}^{-1}$  [28,29,63]. These modes are associated with symmetric stretching ( $E_g$ ), symmetric bending ( $B_{1g}$ ) and antisymmetric bending ( $A_{1g}$ ) vibrations of O-Ti-O bonds [28]. The  $B_{1g}$  mode is observed in rutile at  $144\text{ cm}^{-1}$ ,  $E_g$  mode at  $447\text{ cm}^{-1}$ , while the  $612\text{ cm}^{-1}$  peak is assigned to the  $A_{1g}$  mode (Figure 4). An additional broad band appears in rutile at around  $243\text{ cm}^{-1}$ , which might be attributed to disorder-induced scattering or the second-order effect [28]. The spectrum of anatase shows six Raman-active modes as  $1A_{1g}$ ,  $2B_{1g}$  and  $3E_g$  symmetries. The bands at  $142$ ,  $195$  and  $637\text{ cm}^{-1}$  are assigned to the  $E_g$  modes, while the  $394\text{ cm}^{-1}$  peak is attributed to the  $B_{1g}$  mode. The Raman line at  $514\text{ cm}^{-1}$  in anatase is a doublet of the  $A_{1g}$  and  $B_{1g}$  vibrational modes [29,63,64].

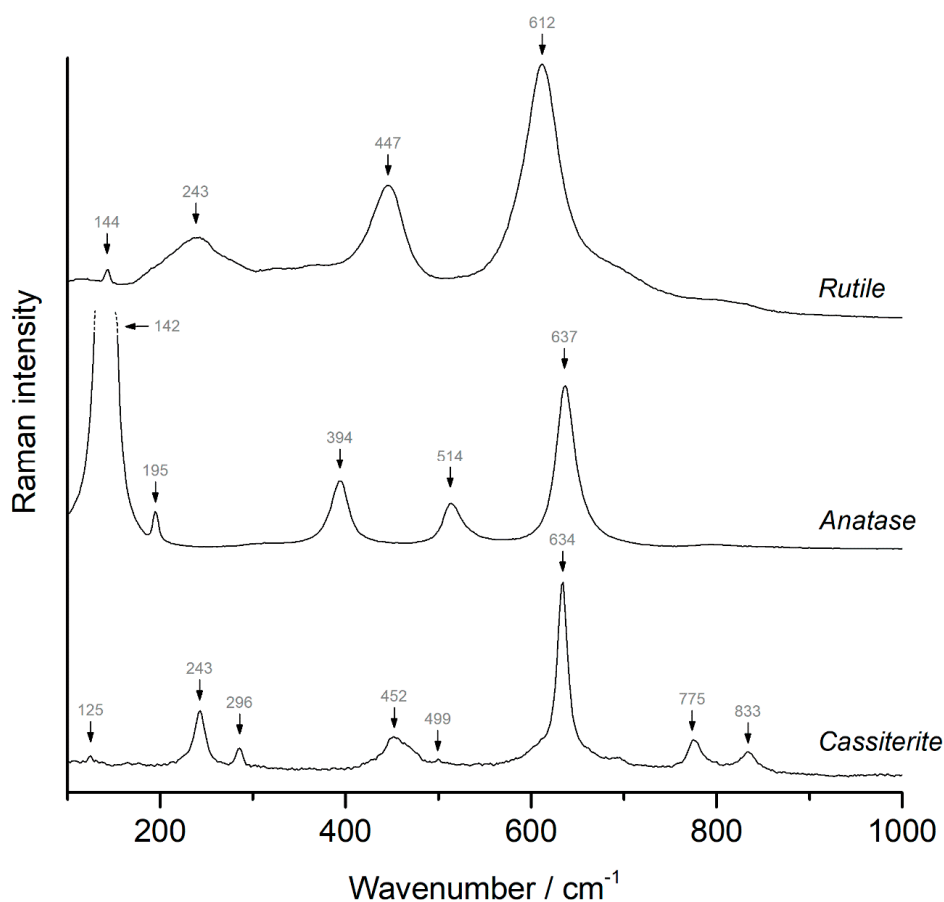


Figure 4. The Raman spectra of rutile, anatase and cassiterite.

In the case of cassiterite, group theory predicts four Raman-active modes. Several Raman bands are observed (Figure 4), out of which the most intense one at  $634\text{ cm}^{-1}$  is assigned to the  $A_{1g}$  mode. The other modes appear at  $125\text{ cm}^{-1}$  ( $B_{1g}$  mode),  $452\text{ cm}^{-1}$  ( $E_g$  mode), and  $775\text{ cm}^{-1}$  ( $B_{2g}$  mode) [27,65,66]. Two additional bands are observed at  $499$  and  $833\text{ cm}^{-1}$ . The Raman lines at  $243$  and  $286\text{ cm}^{-1}$  are attributed to the transverse (TO) and longitudinal optical (LO) modes, respectively [27].

#### 4.5. Titanite and Barite

Titanite ( $\text{CaTiSiO}_5$ ) is a nesosilicate with a structure composed of  $\text{SiO}_4$  tetrahedra,  $\text{TiO}_6$  octahedra and  $\text{CaO}_7$  polyhedra (Figure S11). The Ti atoms are in an off-centered position within the octahedra.  $\text{TiO}_6$  octahedra share corners, forming zig-zag chains that are linked by  $\text{SiO}_4$  units. The entire framework contains large cavities that enclose the Ca atoms [67,68].

The Raman spectrum of titanite (Figure 5) shows multiple bands that are rather broad and sometimes asymmetric. The band assignment considers the strong influence of the Ti-O bonds, which show a stretching mode at  $608\text{ cm}^{-1}$ . The vibrational modes of  $\text{SiO}_4$  tetrahedra are visible at  $859$  and  $871\text{ cm}^{-1}$  for the symmetric stretching  $\nu_1$  and at  $913\text{ cm}^{-1}$  for the  $\nu_3$  antisymmetric stretch. Three other intense lines appear at  $423$ ,  $468$  and  $541\text{ cm}^{-1}$  that can be assigned to the  $\nu_4$  bending modes [69,70]. Up to 10 more bands appear in the low region of the spectrum, which are attributed to the external modes (Figure 5).

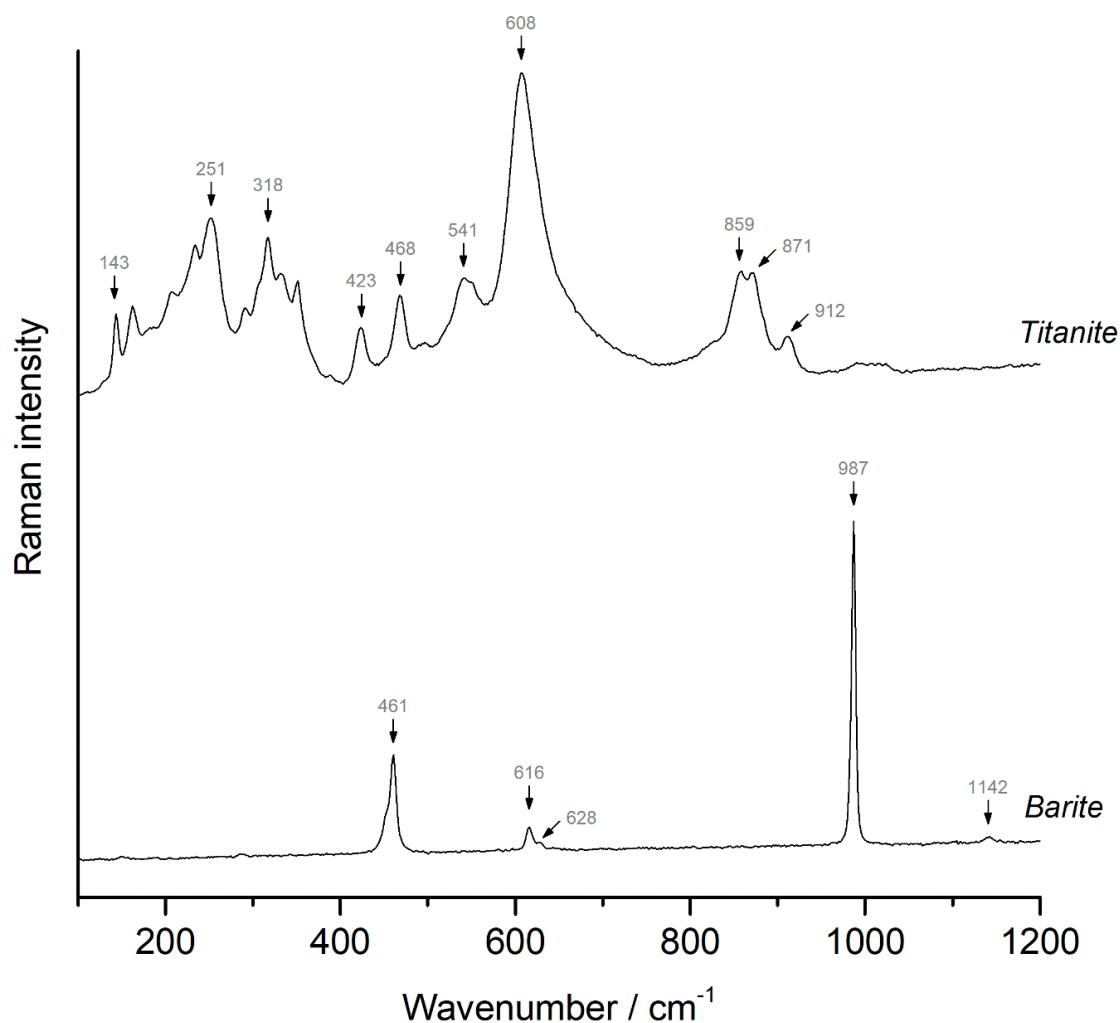


Figure 5. The Raman spectra of titanite and barite.

As in the case of zircon, titanite can be affected by metamictization due to its relatively high contents of REE, U, and Th. Zhang et al. [68] showed that the Raman spectrum of titanite is strongly dependent on the degree of metamictization and it changes by broadening peaks, shifting frequencies, decreasing overall intensity and new additional bands.

Barite ( $\text{BaSO}_4$ ) is a sulfate mineral with  $\text{SO}_4$  tetrahedra as fundamental unit that surround the  $\text{Ba}^{2+}$  cations (Figure S12). The Raman spectrum of barite (Figure 5) shows very clear and sharp bands that can be attributed to the four fundamental vibrational modes of  $\text{SO}_4$  tetrahedra. Therefore, the most intense line at  $987\text{ cm}^{-1}$  is assigned to the  $\nu_1$  stretching mode and the very weak one at  $1142\text{ cm}^{-1}$  is due to the  $\nu_3$  mode. The bending vibrations occur at  $461\text{ cm}^{-1}$  for the  $\nu_2$  symmetric type and at  $616$  and  $628\text{ cm}^{-1}$  for the  $\nu_4$  antisymmetric modes [22,23].

## 5. Conclusions

The micro-Raman technique proved to be a powerful tool for identifying a large number of heavy minerals in a typical gold placer deposit from Pianu Valley, Romania. The following minerals were observed: garnet, kyanite, staurolite, zircon, allanite, monazite, xenotime, rutile, anatase, cassiterite, titanite and barite. The results were confirmed by EPMA chemical analysis. Even if Raman spectroscopy can be used as a stand-alone technique for most of the minerals, in some cases it is recommended to use additional techniques for extra caution in structural and chemical interpretation of the minerals.

Systematic shifting of the Raman bands is very sensitive to structural deformations, even at a low degree of cation substitutions, especially for solid solution series. Such shifting behavior was observed in garnets, kyanite, staurolite and zircon. Several Raman bands in garnets spectra are strongly correlated with the average ionic radius in the  $X^{2+}$  site and therefore peaks positions are dependent to the molar ratios of each end-member. The chemical composition of intermediate members can be estimated by considering up to six peaks with unimodal behavior only by means of Raman spectroscopy.

The distinction between polymorphic minerals can be realized only by structural investigations, micro-Raman being the fastest way to obtain such information. This approach was successfully used complementary to chemical analyses in order to differentiate between kyanite-sillimanite-andalusite and titanium dioxide polymorphs (rutile-anatase-brookite).

Metamictization processes can affect some important accessory minerals due to their relatively high contents of U and Th radioactive elements. The degree of radiation damage can be assessed by evaluating the Raman spectra. Features like broad peaks, frequency shifting and lower intensities are directly correlated with the metamictization degree in zircon, titanite and monazite, even if the latter is more resistant to radioactive damage.

**Supplementary Materials:** The following are available online at <http://www.mdpi.com/2075-163X/10/11/988/s1>, Figure S1: Crystal structure of garnets, Figure S2: Crystal structure of kyanite, Figure S3: Crystal structure of staurolite, Figure S4: Crystal structure of zircon, Figure S5: Crystal structure of allanite-(Ce), Figure S6: Crystal structure of monazite, Figure S7: Crystal structure of xenotime-(Y), Figure S8: Crystal structure of rutile, Figure S9: Crystal structure of anatase, Figure S10: Crystal structure of cassiterite, Figure S11: Crystal structure of titanite, Figure S12: Crystal structure of barite, Table S1: Chemical composition of the studied garnets, Table S2: Chemical composition of the studied kyanite and staurolite samples, Table S3: Chemical composition of zircons, Table S4: Chemical composition of REE minerals (allanite, monazite and xenotime), Table S5: Selective chemical compositions of rutile, anatase, cassiterite, titanite and barite.

**Author Contributions:** Conceptualization, A.E.M. and A.B.; methodology, A.E.M., A.B., G.D. and A.I.A.; software, A.B.; validation, G.D., N.B. and H.G.D.; formal analysis, A.E.M. and A.B.; investigation, A.E.M., A.B., and A.I.A.; resources, A.E.M., G.D. and N.B.; data curation, A.B.; writing—original draft preparation, A.E.M.; writing—review and editing, A.B. and H.G.D.; visualization, A.B.; supervision, G.D., N.B. and H.G.D.; project administration, A.E.M.; funding acquisition, A.E.M. All authors have read and agreed to the published version of the manuscript.

**Funding:** This work was supported by a grant of the “Alexandru Ioan Cuza” University of Iasi, within the Research Grants program, Grant UAIC, code GI-UAIC-2018-02.

**Acknowledgments:** The authors are grateful to the staff of Earth Science Institute of the Slovak Academy of Sciences (Banská Bystrica, Slovakia) for facilitating the access to EPMA and micro-Raman laboratories. We extend our gratitude also to the anonymous reviewers for their time spent reading the first draft of our manuscript and for the valuable suggestions.

**Conflicts of Interest:** The authors declare no conflict of interest.

## References

- Dill, H. A review of heavy minerals in clastic sediments with case studies from the alluvial-fan through the nearshore-marine environments. *Earth Sci. Rev.* **1998**, *45*, 103–132. [[CrossRef](#)]
- Dill, H.G.; Goldmann, S.; Cravero, F. Zr-Ti-Fe placers along the coast of NE Argentina: Provenance analysis and ore guide for the metallogensis in the South Atlantic Ocean. *Ore Geol. Rev.* **2018**, *95*, 131–160. [[CrossRef](#)]
- Maftai, A.E.; Dill, H.G.; Buzatu, A.; Iancu, G.; Buzgar, N.; Andráš, P. Chemical and mineralogical composition of fluvial sediments (Bistrita River, Romania): Geogenic vs. anthropogenic input into rivers on its way through mining areas. *Geochemistry* **2018**, *78*, 385–395. [[CrossRef](#)]
- Mange, M.A.; Morton, A.C. Geochemistry of Heavy Minerals. In *Developments in Sedimentology*; Elsevier BV: Amsterdam, The Netherlands, 2007; Volume 58, pp. 345–391.
- Sevastjanova, I.; Hall, R.; Alderton, D. A detrital heavy mineral viewpoint on sediment provenance and tropical weathering in SE Asia. *Sediment. Geol.* **2012**, *280*, 179–194. [[CrossRef](#)]
- Ali, M.Y.; Hibberd, P.; Stoikovich, B. Origin and prospectivity of heavy mineral enriched sand deposits along the Somaliland coastal areas. *J. Afr. Earth Sci.* **2018**, *140*, 60–75. [[CrossRef](#)]
- Dill, H.G. Gems and Placers—A Genetic Relationship Par Excellence. *Minerals* **2018**, *8*, 470. [[CrossRef](#)]
- Williams, G.; Gilman, S.K.; Marlowe, Z. *Geometallurgy in Mineral Sands Deposits—Linking Geological Artifacts to Metallurgy and Mine Planning*; The Australasian Institute of Mining and Metallurgy: Carlton, VI, Australia, 2011; pp. 383–392.
- Li, G.; Yan, W.; Zhong, L.; Xia, Z.; Wang, S. Provenance of heavy mineral deposits on the northwestern shelf of the South China Sea, evidence from single-mineral chemistry. *Mar. Geol.* **2015**, *363*, 112–124. [[CrossRef](#)]
- Nyobe, J.M.; Sababa, E.; Bayiga, E.C.; Ndjigui, P.-D. Mineralogical and geochemical features of alluvial sediments from the Lobo watershed (Southern Cameroon): Implications for rutile exploration. *Comptes Rendus Geosci.* **2018**, *350*, 119–129. [[CrossRef](#)]
- Pirkle, F.L.; Pirkle, W.A.; Pirkle, E. Heavy-Mineral Sands of the Atlantic and Gulf Coastal Plains, USA. In *Developments in Sedimentology*; Elsevier BV: Amsterdam, The Netherlands, 2007; Volume 58, pp. 1144–1232.
- Smith, E.; Dent, G. *Modern Raman Spectroscopy—A Practical Approach*; Wiley: Hoboken, NJ, USA, 2004.
- Worobiec, A.; Stefaniak, E.A.; Potgieter-Vermaak, S.; Sawlowicz, Z.; Spolnik, Z.; Van Grieken, R. Characterisation of concentrates of heavy mineral sands by micro-Raman spectrometry and CC-SEM/EDX with HCA. *Appl. Geochem.* **2007**, *22*, 2078–2085. [[CrossRef](#)]
- Chew, D.; O’Sullivan, G.; Caracciolo, L.; Mark, C.; Tyrrell, S. Sourcing the sand: Accessory mineral fertility, analytical and other biases in detrital U-Pb provenance analysis. *Earth Sci. Rev.* **2020**, *202*, 103093. [[CrossRef](#)]
- Lünsdorf, N.K.; Kalies, J.; Ahlers, P.; Dunkl, I.; Von Eynatten, H. Semi-Automated Heavy-Mineral Analysis by Raman Spectroscopy. *Minerals* **2019**, *9*, 385. [[CrossRef](#)]
- Bersani, D.; Andò, S.; Vignola, P.; Moltifiori, G.; Marino, I.-G.; Lottici, P.P.; Diella, V. Micro-Raman spectroscopy as a routine tool for garnet analysis. *Spectrochim. Acta Part A Mol. Biomol. Spectrosc.* **2009**, *73*, 484–491. [[CrossRef](#)]
- Smith, D.C. The RAMANITA© method for non-destructive and in situ semi-quantitative chemical analysis of mineral solid-solutions by multidimensional calibration of Raman wavenumber shifts. *Spectrochim. Acta Part A Mol. Biomol. Spectrosc.* **2005**, *61*, 2299–2314. [[CrossRef](#)]
- Titorenkova, R.; Mihailova, B.; Konstantinov, L. Raman spectroscopic study of variably recrystallized metamict zircon from amphibolite-facies metagranites, Serbo-Macedonian massif, Bulgaria. *Can. Miner.* **2006**, *44*, 1357–1366. [[CrossRef](#)]
- Zhai, K.; Xue, W.; Wang, H.; Wu, X.; Zhai, S. Raman spectra of sillimanite, andalusite, and kyanite at various temperatures. *Phys. Chem. Miner.* **2020**, *47*, 1–11. [[CrossRef](#)]
- Ruschel, K.; Nasdala, L.; Kronz, A.; Hanchar, J.M.; Töbrens, D.M.; Škoda, R.; Finger, F.; Möller, A. A Raman spectroscopic study on the structural disorder of monazite-(Ce). *Miner. Pet.* **2012**, *105*, 41–55. [[CrossRef](#)]

21. Silva, E.; Ayala, A.; Guedes, I.; Paschoal, C.; Moreira, R.; Loong, C.-K.; Boatner, L. Vibrational spectra of monazite-type rare-earth orthophosphates. *Opt. Mater.* **2006**, *29*, 224–230. [[CrossRef](#)]
22. Buzatu, A.; Dill, H.G.; Buzgar, N.; Damian, G.; Maftei, A.E.; Apopei, A.I. Efflorescent sulfates from Baia Sprie mining area (Romania)—Acid mine drainage and climatological approach. *Sci. Total. Environ.* **2016**, *542*, 629–641. [[CrossRef](#)]
23. Buzgar, N.; Buzatu, A.; Sanislav, I.V. The Raman study on certain sulfates. *An. St. Univ. Al. I. Cuza Iasi Geol.* **2009**, *1*, 5–23.
24. Apopei, A.I.; Damian, G.; Buzgar, N.; Buzatu, A. Mineralogy and geochemistry of Pb–Sb/As-sulfosalts from Coranda-Hondol ore deposit (Romania)—Conditions of telluride deposition. *Ore Geol. Rev.* **2016**, *72*, 857–873. [[CrossRef](#)]
25. Apopei, A.I.; Damian, G.; Buzgar, N.; Buzatu, A.; Andráš, P.; Milovská, S. The determination of the Sb/As content in natural tetrahedrite–tennantite and bournonite–seligmannite solid solution series by Raman spectroscopy. *Min. Mag.* **2017**, *81*, 1439–1456. [[CrossRef](#)]
26. Buzatu, A.; Damian, G.; Buzgar, N.; Andráš, P.; Apopei, A.I.; Maftei, A.E.; Milovska, S. Structural key features of bismuth and Sb–As sulfosalts from hydrothermal deposits—micro-Raman spectrometry. *Vib. Spectrosc.* **2017**, *89*, 49–56. [[CrossRef](#)]
27. Diéguez, A.; Rodríguez, A.R.; Vilà, A.; Morante, J.R. The complete Raman spectrum of nanometric SnO<sub>2</sub> particles. *J. Appl. Phys.* **2001**, *90*, 1550–1557. [[CrossRef](#)]
28. Ekoi, E.; Gowen, A.; Dorrepaal, R.; Dowling, D. Characterisation of titanium oxide layers using Raman spectroscopy and optical profilometry: Influence of oxide properties. *Results Phys.* **2019**, *12*, 1574–1585. [[CrossRef](#)]
29. Frank, O.; Zukalova, M.; Laskova, B.; Kürti, J.; Koltai, J.; Kavan, L. Raman spectra of titanium dioxide (anatase, rutile) with identified oxygen isotopes (16, 17, 18). *Phys. Chem. Chem. Phys.* **2012**, *14*, 14567–14572. [[CrossRef](#)]
30. Nakamoto, K. *Infrared and Raman Spectra of Inorganic and Coordination Compounds Part A: Theory and Applications in Inorganic Chemistry*; John Wiley and Sons: New Jersey, NJ, USA, 2009.
31. Bedelea, H.; Bedelea, A. Contributions to the Study of the Alluvial Gold from Valea Pianului Area (Alba District). *Stud. Univ. Babeş-Bolyai, Geol.* **2001**, *46*, 161–169. [[CrossRef](#)]
32. Udubaşa, G.; Udubaşa, S.S. Native platinum in Romania: The single occurrence—Pianu Valley, Sebeş Mts. *Pangea* **2015**, *15*, 5–8.
33. Saulea Bococ, E. The mineralogical constitution of the alluvial sand from Pianu de sus, Alba District, Romania. *An. Sci. Univ. Iasi* **1934**, *9*, 514–523.
34. Udubaşa, G.; Pop, D.; Costea, C. Native platinum at Pianu, Sebeş county, Romania. *Rom. J. Min. Dep.* **2004**, *81*, 192–194.
35. Săndulescu, M. *Geotectonics of Romania*; Ed. Tehnică: Bucureşti, Romania, 1984. (In Romanian)
36. Popa, S.; Popa, T.; Jianu, A.; Puiu, S.; Franchi, R.; Gobbi, L.; Puglisi, D. Preliminary data about the chemical composition of alluvial gold from Pianu Valley (Sebeş Mountains, Southern Carpathians, Romania). *Proc. Rom. Acad.* **2006**, *1*, 17–21.
37. Iancu, V.; Berza, T.; Seghedi, A.; Marunţiu, M. Palaeozoic rock assemblages incorporated in the South Carpathian alpine thrust belt (Romania and Serbia): A review. *Geol. Belg.* **2005**, *8*, 48–68.
38. Iancu, V.; Seghedi, A. The South Carpathians: Tectono-metamorphic units related to Variscan and Pan-African inheritance. *Geo. Eco. Marina* **2017**, *23*, 245–262.
39. Cristea-Stan, D.; Constantinescu, B.; Udubaşa, S.S.; Udubaşa, G. Alluvial gold in the South Carpathians: Analytical data on some new occurrences. *Rom. J. Min. Dep.* **2016**, *89*, 35–40.
40. Stoica, A.M.; Ducea, M.N.; Roban, R.D.; Jianu, D. Origin and evolution of the South Carpathians basement (Romania): A zircon and monazite geochronologic study of its Alpine sedimentary cover. *Int. Geol. Rev.* **2015**, *58*, 510–524. [[CrossRef](#)]
41. Grew, E.S.; Locock, A.J.; Mills, S.J.; Galuskina, I.O.; Galuskin, E.V.; Hålenius, U. Nomenclature of the garnet supergroup. *Am. Miner.* **2013**, *98*, 785–811. [[CrossRef](#)]
42. Deer, F.W.A.; Howie, R.A.; Zussman, J. *An Introduction to the Rock-Forming Minerals*; Mineralogical Society: London, UK, 2013; Volume 1A.
43. Mingsheng, P.; Mao, H.K.; Dien, L.; Chao, E.C.T. Raman spectroscopy of garnet-group minerals. *Chin. J. Geochem.* **1994**, *13*, 176–183. [[CrossRef](#)]

44. Hofmeister, A.M.; Chopelas, A. Vibrational spectroscopy of end-member silicate garnets. *Phys. Chem. Miner.* **1991**, *17*, 503–526. [[CrossRef](#)]
45. Kolesov, B.A.; Geiger, C.A. Raman spectra of silicate garnets. *Phys. Chem. Miner.* **1998**, *25*, 142–151. [[CrossRef](#)]
46. Kos, S.; Dolenc, M.; Lux, J.; Dolenc, S. Raman Microspectroscopy of Garnets from S-Fibulae from the Archaeological Site Lajh (Slovenia). *Minerals* **2020**, *10*, 325. [[CrossRef](#)]
47. Makreski, P.; Jovanovski, G.; Stojančeska, S. Minerals from Macedonia XIII: Vibrational spectra of some commonly appearing nesosilicate minerals. *J. Mol. Struct.* **2005**, *79*–92. [[CrossRef](#)]
48. Kolesov, B.A.; Geiger, C.A.; Armbruster, T. The dynamic properties of zircon studied by single-crystal X-ray diffraction and Raman spectroscopy. *Eur. J. Miner.* **2001**, *13*, 939–948. [[CrossRef](#)]
49. Zhang, M.; Salje, E.; Farnan, I.; Graeme-Barber, A.; Daniel, P.; Ewing, R.C.; Clark, A.M.; Leroux, H. Metamictization of zircon: Raman spectroscopic study. *J. Physics: Condens. Matter* **2000**, *12*, 1915–1925. [[CrossRef](#)]
50. Bouvier, A.-S.; Ushikubo, T.; Kita, N.T.; Cavosie, A.J.; Kozdon, R.; Valley, J.W. Li isotopes and trace elements as a petrogenetic tracer in zircon: Insights from Archean TTGs and sanukitoids. *Contrib. Miner. Pet.* **2011**, *163*, 745–768. [[CrossRef](#)]
51. López, A.; Frost, R.L. Identification of allanite (Ce, Ca, Y)<sub>2</sub>(Al, Fe<sup>3+</sup>)<sub>3</sub>(SiO<sub>4</sub>)<sub>3</sub>OH found in marble from Chillagoe, Queensland using Raman spectroscopy. *Spectrochim. Acta Part A Mol. Biomol. Spectrosc.* **2015**, *138*, 229–233. [[CrossRef](#)]
52. Švecová, E.; Čopjaková, R.; Losos, Z.; Škoda, R.; Nasdala, L.; Cícha, J. Multi-stage evolution of xenotime-(Y) from Písek pegmatites, Czech Republic: An electron probe micro-analysis and Raman spectroscopy study. *Miner. Pet.* **2016**, *110*, 747–765. [[CrossRef](#)]
53. Anderson, A.J.; Hanchar, J.M.; Hodges, K.V.; Van Soest, M.C. Mapping radiation damage zoning in zircon using Raman spectroscopy: Implications for zircon chronology. *Chem. Geol.* **2020**, *538*, 119494. [[CrossRef](#)]
54. Kaulina, T.; Lyalina, L.; Kamenetsky, V.; Il'chenko, V.; Bocharov, V.; Gannibal, M. Composition and Structure of Zircon from Hydrothermal Uranium Occurrences of the Litsa Ore Area (Kola Region, Russia). *Geosciences* **2020**, *10*, 278. [[CrossRef](#)]
55. Dawson, P.; Hargreave, M.M.; Wilkinson, G.R. The vibrational spectrum of zircon (ZrSiO<sub>4</sub>). *J. Phys. C Solid State Phys.* **1971**, *4*, 240–256. [[CrossRef](#)]
56. Dill, H.; Weber, B. Accessory minerals of fluorite and their implication regarding the environment of formation (Nabburg–Wölsendorf fluorite district, SE Germany), with special reference to fetid fluorite (“Stinkspat”). *Ore Geol. Rev.* **2010**, *37*, 65–86. [[CrossRef](#)]
57. Varlamov, D.A.; Ermolaeva, V.N.; Chukanov, N.V.; Jančev, S.; Vígasina, M.F.; Plechov, P.Y. New Data on Epidote-Supergroup Minerals: Unusual Chemical Compositions, Typochemistry, and Raman Spectroscopy. *Geol. Ore Deposits* **2019**, *61*, 827–842. [[CrossRef](#)]
58. Chukanov, N.V.; Vígasina, M.F. *Vibrational (Infrared and Raman) Spectra of Minerals and Related Compounds*; Springer International Publishing: New York, NY, USA, 2020.
59. Makreski, P.; Jovanovski, G.; Kaitner, B.; Gajović, A.; Biljan, T. Minerals from Macedonia. *Vib. Spectrosc.* **2007**, *44*, 162–170. [[CrossRef](#)]
60. Clavier, N.; Mesbah, A.; Szenknect, S.; Dacheux, N. Monazite, rhabdophane, xenotime & churchite: Vibrational spectroscopy of gadolinium phosphate polymorphs. *Spectrochim. Acta Part A Mol. Biomol. Spectrosc.* **2018**, *205*, 85–94. [[CrossRef](#)]
61. Wu, L.-G.; Li, C.-F.; Ling, X.-X.; Yang, Y.-H.; Mao, Q.; Putlitz, B. Further Characterization of the RW-1 Monazite: A New Working Reference Material for Oxygen and Neodymium Isotopic Microanalysis. *Minerals* **2019**, *9*, 583. [[CrossRef](#)]
62. Begun, G.M.; Beall, G.W.; Boatner, L.A.; Gregor, W.J. Raman spectra of the rare earth orthophosphates. *J. Raman Spectrosc.* **1981**, *11*, 273–278. [[CrossRef](#)]
63. Balachandran, U.; Eror, N. Raman spectra of titanium dioxide. *J. Solid State Chem.* **1982**, *42*, 276–282. [[CrossRef](#)]
64. Sekiya, T.; Ohta, S.; Kamei, S.; Hanakawa, M.; Kurita, S. Raman spectroscopy and phase transition of anatase TiO<sub>2</sub> under high pressure. *J. Phys. Chem. Solids* **2001**, *62*, 717–721. [[CrossRef](#)]
65. Beattie, I.R.; Gilson, T.R. Single crystal laser Raman spectroscopy. *Proc. R. Soc. London Ser. A Math. Phys. Sci.* **1968**, *307*, 407–429. [[CrossRef](#)]
66. Scott, J.F. Raman Spectrum of SnO<sub>2</sub>. *J. Chem. Phys.* **1970**, *53*, 852–853. [[CrossRef](#)]



67. Heller, B.M.; Lünsdorf, N.K.; Dunkl, I.; Molnár, F.; Von Eynatten, H. Estimation of radiation damage in titanites using Raman spectroscopy. *Am. Miner.* **2019**, *104*, 857–868. [[CrossRef](#)]
68. Zhang, M.; Salje, E.; Redfern, S.A.; Bismayer, U.; Groat, L.A. Intermediate structures in radiation damaged titanite (CaTiSiO<sub>5</sub>): A Raman spectroscopic study. *J. Physics: Condens. Matter* **2013**, *25*, 115–402. [[CrossRef](#)]
69. Heyns, A.M.; Harden, P.M. The temperature dependence of the Raman spectra of chromium-doped titanite (CaTiOSiO<sub>4</sub>). *J. Raman Spectrosc.* **2013**, *44*, 1615–1624. [[CrossRef](#)]
70. Salje, E.; Schmidt, C.; Bismayer, U. Structural phase transition in titanite, CaTiSiO<sub>5</sub>: A ramanspectroscopic study. *Phys. Chem. Miner.* **1993**, *19*, 502–506. [[CrossRef](#)]

**Publisher’s Note:** MDPI stays neutral with regard to jurisdictional claims in published maps and institutional affiliations.



© 2020 by the authors. Licensee MDPI, Basel, Switzerland. This article is an open access article distributed under the terms and conditions of the Creative Commons Attribution (CC BY) license (<http://creativecommons.org/licenses/by/4.0/>).